

## Kinetic instabilities in the lunar wake: ARTEMIS observations

J. B. Tao,<sup>1</sup> R. E. Ergun,<sup>1</sup> D. L. Newman,<sup>2</sup> J. S. Halekas,<sup>3</sup> L. Andersson,<sup>1</sup> V. Angelopoulos,<sup>4</sup> J. W. Bonnell,<sup>3</sup> J. P. McFadden,<sup>3</sup> C. M. Cully,<sup>5</sup> H.-U. Auster,<sup>6</sup> K.-H. Glassmeier,<sup>6</sup> D. E. Larson,<sup>3</sup> W. Baumjohann,<sup>7</sup> and M. V. Goldman<sup>2</sup>

Received 10 November 2011; revised 3 February 2012; accepted 6 February 2012; published 28 March 2012.

[1] The Acceleration, Reconnection, Turbulence and Electrodynamics of the Moon's Interaction with the Sun (ARTEMIS) mission is a new two-probe lunar mission derived from the Time History of Events and Macroscale Interactions during Substorms (THEMIS) mission. On 13 February 2010, one of the two probes, ARTEMIS P1 (formerly THEMIS-B), made the first lunar wake flyby of the mission. We present detailed analysis of the electrostatic waves observed on the outbound side of the flyby that were associated with electron beams. Halekas et al. (2011) derived a net potential across the lunar wake from observations and suggested that the net potential generated the observed electron beams and the electron beams in turn excited the observed electrostatic waves due to kinetic instabilities. The wavelengths and velocities of the electrostatic waves are estimated, using high-resolution electric field instrument data with cross-spectrum analysis and cross-correlation analysis. In general, the estimated wavelengths vary from a few hundred meters to a couple of thousand meters. The estimated phase velocities are on the order of  $1000 \text{ km s}^{-1}$ . In addition, we perform 1-D Vlasov simulations to help identify the mode of the observed electrostatic waves. We conclude that the observed electrostatic waves are likely on the electron beam mode branch.

**Citation:** Tao, J. B. et al. (2012), Kinetic instabilities in the lunar wake: ARTEMIS observations, *J. Geophys. Res.*, 117, A03106, doi:10.1029/2011JA017364.

### 1. Introduction

[2] When the Moon is immersed in the solar wind, solar wind plasmas that impinge on the Moon are absorbed by the lunar surface, creating a depleted wake region downstream, which is referred to as the lunar wake. Unlike the Earth, the Moon does not have an intrinsic magnetic field, and hence it has no magnetosphere. In addition, the conductivity of the Moon is sufficiently low that the motion of the solar wind magnetic field does not induce a significant diamagnetic field. Therefore, unlike solar wind plasmas, the solar wind magnetic field penetrates the Moon with little disturbance [Ness et al., 1967; Ness, 1972].

[3] The density gradient between the lunar wake and the solar wind drives solar wind plasmas to refill the lunar wake along magnetic field lines. Ions and electrons undergo ambipolar diffusion during the refilling, in which electrons rush into the wake ahead of ions causing the wake to become negatively charged. The potential gradient in the wake in turn sets up an ambipolar electric field that accelerates ions into the wake. Since the field-aligned distribution of electrons are altered by the wake potential, kinetic instabilities are expected to take place inside the wake.

[4] Early studies of the lunar wake were mostly based on observations from the U.S. Explorer 35 and the Apollo program in the 1960s and 1970s (see Ness [1972] and Schubert and Lichtenstein [1974] for review). The Wind spacecraft swung by the lunar wake at roughly  $7 R_L$  (lunar radius) downstream from the Moon for a gravity assist and provided observations of the wake with modern plasma instruments [Ogilvie et al., 1996; Owen et al., 1996; Farrell et al., 1996; Kellogg et al., 1996; Bosqued et al., 1996], which drove a series of investigations of the dynamics associated with the lunar wake [Bale et al., 1997; Bale, 1997; Farrell et al., 1998; Birch and Chapman, 2001a, 2001b, 2002; Nakagawa et al., 2003; Kallio, 2005]. Among recent lunar missions, the Acceleration, Reconnection, Turbulence and Electrodynamics of the Moon's Interaction with the Sun (ARTEMIS) mission [Angelopoulos, 2010], which is derived from the two outermost satellites (known as P1

<sup>1</sup>Laboratory for Atmospheric and Space Physics, University of Colorado at Boulder, Boulder, Colorado, USA.

<sup>2</sup>Center for Integrated Plasma Studies, University of Colorado at Boulder, Boulder, Colorado, USA.

<sup>3</sup>Space Sciences Laboratory, University of California, Berkeley, California, USA.

<sup>4</sup>IGPP/ESS, University of California, Los Angeles, California, USA.

<sup>5</sup>Swedish Institute of Space Physics, Uppsala, Sweden.

<sup>6</sup>Institut für Geophysik und Extraterrestrische Physik, Technische Universität Braunschweig, Braunschweig, Germany.

<sup>7</sup>Space Research Institute, Austrian Academy of Sciences, Graz, Austria.

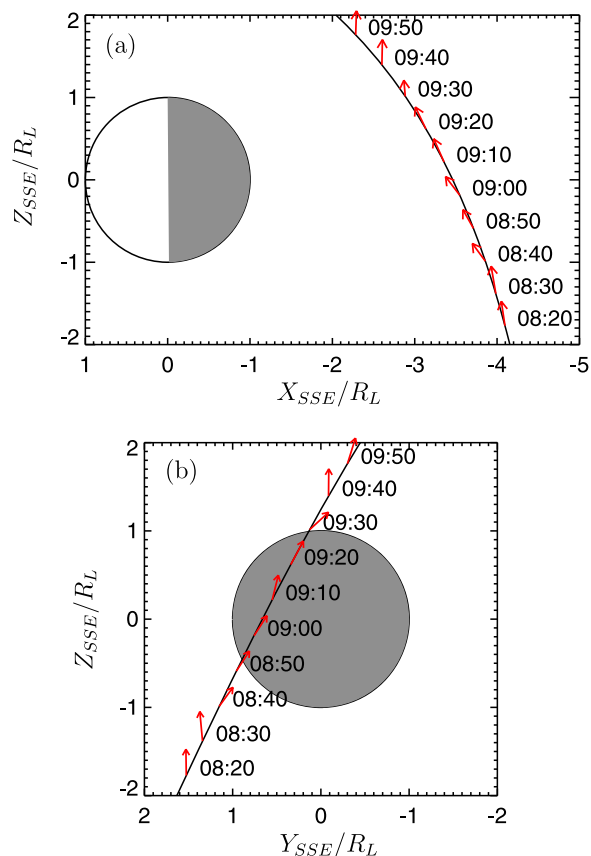


**Figure 1.** The trajectory of ARTEMIS P1 during its first lunar wake flyby on 13 February 2010 in the (a)  $x$ - $z$  plane and (b)  $y$ - $z$  plane of the Selenocentric Solar Ecliptic (SSE) coordinate system. (The SSE system is similar to the GSE system, with the origin at the center of the Moon and the  $x$  axis pointing to the Sun.) The coordinates are normalized by the lunar radius ( $1R_L \approx 1737$  km). The circles centered at the origins represent the Moon, where the gray areas represent the nightside of the Moon. The red vectors indicate the observed magnetic field at the times (UT) labeled on the right, whose lengths are scaled with respect to the magnitude of the magnetic field ( $\sim 6$  nT) at 08:20 UT. The magnetic field data are from the onboard fluxgate magnetometer (FGM) [Auster *et al.*, 2008].

and P2, or THB and THC) of the Time History of Events and Macroscale Interactions during Substorms (THEMIS) mission [Angelopoulos, 2008], is able to cover an extensive range of the lunar wake ( $\sim 1.1$ – $12 R_L$  selenocentric after lunar orbit insertion). Other missions, including the Lunar Prospector, SMART-1, Kaguya, Change’e 1 and 2, Chandrayaan-1, and the Lunar Reconnaissance Orbiter, are generally low-altitude orbiters.

[5] During the transition from orbiting the Earth to orbiting the Moon, the ARTEMIS P1 spacecraft made the first lunar wake flyby of the mission  $\sim 3.5 R_L$  downstream from the Moon on 13 February 2010, during which the Moon was immersed in the solar wind at  $\sim (63, -9, 2.5) R_E$  in GSE coordinates. (Universal time (UT) is used throughout the paper except otherwise noted.) Detailed observations of magnetic fields and plasma properties during this flyby was

reported by Halekas *et al.* [2011], and a global simulation of this flyby was performed by Wiehle *et al.* [2011].

[6] One particularly interesting aspect of this flyby is that the onboard electric field instrument (EFI) was able to resolve the wavelength and phase velocity of the electrostatic waves observed on the outbound side of the flyby. Wavelength and phase velocity are generally difficult to resolve due to the limited physical length of the electric field instrument booms. Therefore, this flyby offered us a rare opportunity to make a comprehensive understanding of the properties of the observed electrostatic waves, which is important for studying the dynamics of waves and particles in the lunar wake. The techniques we use are cross-spectrum analysis and cross-correlation analysis, which are generally used in deriving wavelength and phase velocity [Labelle and Kintner, 1989; Bonnell, 1997]. Similar previous work includes those by Angelopoulos *et al.* [2001] and Ergun *et al.* [1991]. In addition, we present 1-D Vlasov simulation results to identify the mode of the observed electrostatic waves.

[7] The organization of the rest of the paper is as follows. An overview of the flyby is provided in section 2. Following the presentation of waveform and spectrum measurements in section 3, the wavelengths and phase velocities of the observed electrostatic waves are estimated in section 4. The Vlasov simulation results are presented in section 5. The paper is finalized with a brief discussion and a summary.

## 2. Overview of the Flyby

[8] Figure 1 shows the trajectory of ARTEMIS P1 during the flyby. Figure 2 shows overview observations of the flyby. During the flyby, ARTEMIS P1 experienced a crossing of the lunar shadow, an interval indicated by the two vertical black dashed lines in Figure 2. Because the solar wind velocity is not exactly along the Sun-Moon line, the lunar wake does not overlap the lunar shadow precisely, as can be seen from the ion density in Figure 2a. The ion density, along with other particle data (ion velocity, electron temperature, and electron differential energy flux), is from the electrostatic analyzer (ESA) [McFadden *et al.*, 2008]. The roughly linear slope of the ion density curve in Figure 2a (a log plot) indicates that the ion density decreases exponentially toward inside of the wake, which is consistent with previous theoretical work [Samir *et al.*, 1983]. Figure 2b shows the ion flow velocity of the solar wind, which was relatively stable for this flyby.

[9] Figure 2c shows electron temperature ( $T_e$ ).  $T_e$  was approximately isotropic outside the wake. Inside the wake, both the field-aligned temperature and the perpendicular temperature increased, with the former increasing more. This increase is expected in light of the following consideration: Solar wind electrons generally consist of three components: a cold core, a hot halo, and a field-aligned strahl component [Feldman *et al.*, 1975; Louarn *et al.*, 2009]. The wake potential screens out the cold core significantly, as can be seen from the depletion of low-energy flux (the red color) inside the wake in Figure 2e. Therefore, both  $T_{e\parallel}$  and  $T_{e\perp}$  increase as shown in Figure 2c. The reason why  $T_{e\parallel}$  increases more than  $T_{e\perp}$  may be due to anisotropy in the high-energy components of solar wind electrons.

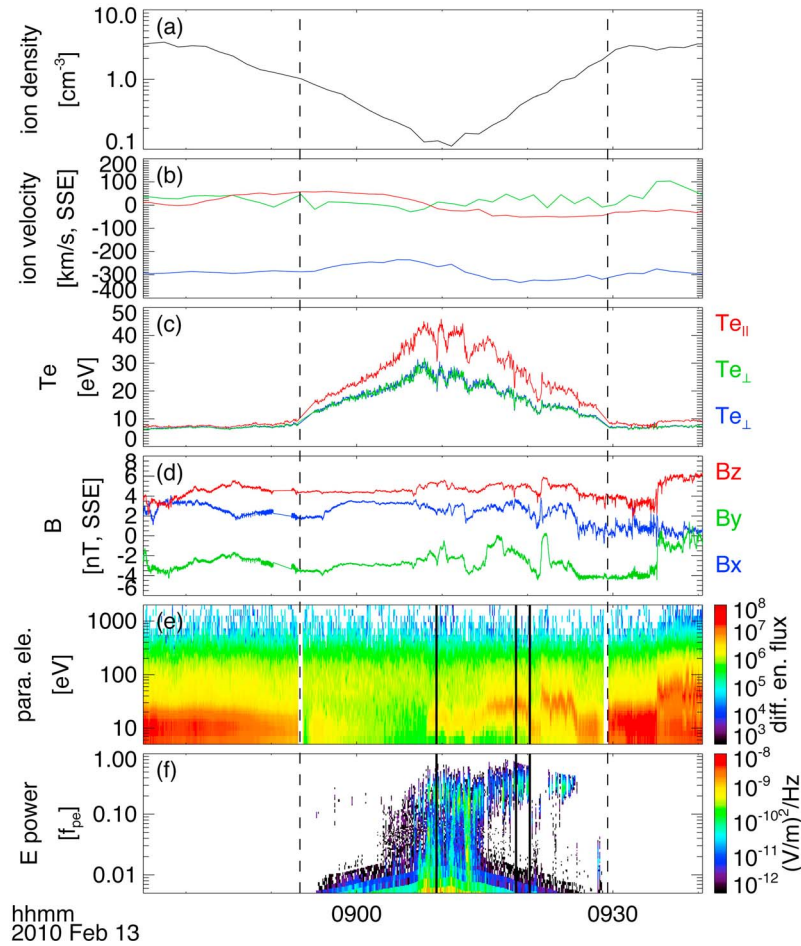


**Figure 2.** Time series overview observations of the flyby, where the shadow interval of the flyby is between the two vertical black dashed lines. (a) Ion density. (b) Ion velocity in SSE coordinates. (c) Electron temperature, where the red line is field-aligned temperature ( $T_{e||}$ ) and the green and blue lines are perpendicular temperatures ( $T_{e\perp}$ ). The blue line is almost fully overlapped by the green line as there is no special preference in perpendicular temperatures. (d) Magnetic field in SSE coordinates. (e) Differential energy flux of parallel electrons. (f) Electric field power spectrum from the onboard digital field board (DFB) [Cully *et al.*, 2008] with frequency normalized by the local electron plasma frequency ( $f_{pe}$ ). The three black vertical bars across Figures 2e and 2f indicate the times of three wave bursts that are analyzed in detail.

[10] The observed magnetic field was mostly stable on the inbound side and had some significant rotations on the outbound side, as shown in Figure 2d.

[11] As indicated by the enhancement of differential energy flux in Figure 2e, parallel electron beams were observed on the outbound side. (The terms “parallel” and “antiparallel” directions are with respect to the ambient magnetic field ( $\mathbf{B}_0$ ), with the former in the same direction of  $\mathbf{B}_0$  and the latter in the opposite direction.  $\mathbf{B}_0$  is determined from measurements with the same temporal resolution as the particle data, namely, a spin period ( $\sim 3$  s).) The parallel electron beams were modulated by the orientation of the magnetic field, which is expected since electrons are primarily restricted to move along field lines due to the frozen-in condition.

[12] Figure 2f shows electric field power spectrum derived by the onboard digital field board (DFB) [Cully

*et al.*, 2008]. There are clear enhancements of electric field power on the outbound side of the flyby (from  $\sim 09:10$  to  $\sim 09:25$  UT) that are correlated with the electron beams shown in Figure 2e. The frequency range of the waves is mostly between  $0.1f_{pe}$  and  $0.4f_{pe}$  except in the middle of the flyby where the power occasionally reaches  $\sim 0.01f_{pe}$ . These waves were identified as electrostatic waves because no corresponding magnetic field signals were observed from the onboard search coil magnetometer (SCM) [Roux *et al.*, 2008]. The properties of these electric field waves are the focus of this paper. The black vertical bars across Figures 2e and 2f indicate the times of three high time resolution wave bursts discussed below. These bursts comprise the *only* high-resolution electric field data associated with the electric field waves in Figure 2f available from this flyby. These data allow us to perform a detailed analysis of these waves. For

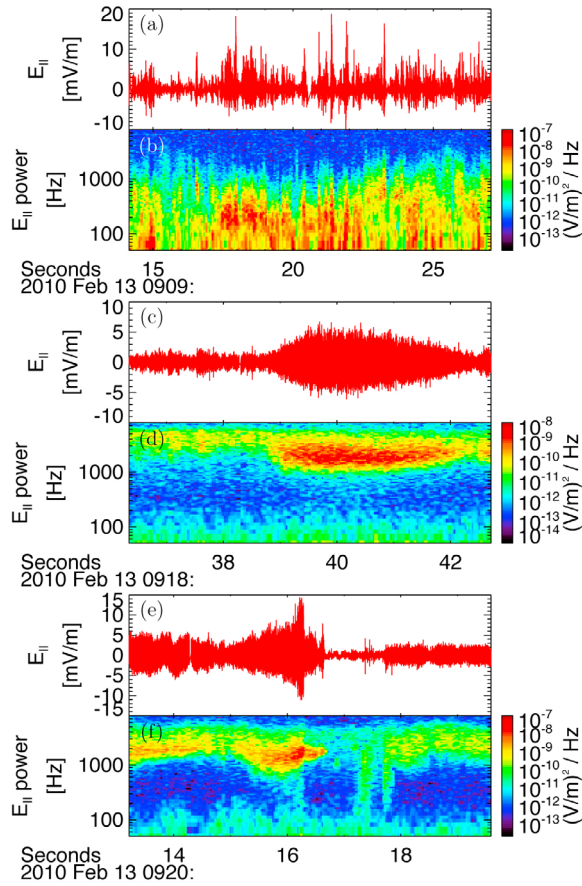


**Figure 3.** Parallel electric field waveforms and spectrograms of (a, b) WB1, (c, d) WB2, and (e, f) WB3.

the ease of reference, these three wave bursts are labeled WB1, WB2, and WB3 in a temporal order.

### 3. Waveform and Spectrum Measurements

[13] Figure 3 displays the waveforms (sample rate  $\sim 16$  kHz; filtered from  $\sim 10$  Hz to  $\sim 6$  kHz) and spectrograms of parallel electric fields ( $E_{\parallel}$ ) from WB1, WB2, and WB3. The waveforms are from the onboard EFI [Bonnell *et al.*, 2008]. The spectrograms were computed from the corresponding waveforms.  $E_{\parallel}$  dominates in the electric field signals of the three wave bursts, indicating that  $\mathbf{E} \parallel \mathbf{B}_0$  and that these electrostatic waves had phase velocity along  $\mathbf{B}_0$ . In general, the  $E_{\parallel}$  amplitudes of these waves roughly vary from 5 to 15  $\text{mV m}^{-1}$  as shown in Figures 3a, 3c, and 3e. The spectral characteristic of these waves, shown in Figures 3b, 3d, and 3f, is generally consistent with that shown in Figure 2f but with detailed structures, especially for WB2 and WB3 which consist of enhanced waves from  $\sim 09:18:39$  to  $\sim 09:18:42$  UT and from  $\sim 09:20:13$  to  $\sim 09:20:16.5$  UT, respectively.

### 4. Wavelength and Phase Velocity Measurements

[14] The onboard EFI consists of three double-probe booms, with two long, orthogonal booms in the spin plane of the spacecraft, and one relatively short boom along the spin

axis [Bonnell *et al.*, 2008]. Because longer booms generally have more accurate measurements [Pedersen *et al.*, 1998], we focus our analysis on measurements from the longest EFI boom which connects the EFI probes numbered 1 and 2. Although not shown, the results from the second longest boom generally confirm those from the longest boom.

[15] Figure 4 illustrates plasma waves passing one EFI boom in the spin plane. In general, the phase of a wave mode with frequency  $\omega$  and wave vector  $\mathbf{k}$  is

$$\theta = \mathbf{k} \cdot \mathbf{x} - \omega t, \quad (1)$$

where  $\theta$  is the phase,  $t$  time,  $\mathbf{x}$  location in 3-D space. As shown in Figure 4, in the EFI frame, the phase shift between the two opposite probes at time  $t$  is

$$\begin{aligned} \Delta\theta(t) &= \theta_1(t) - \theta_2(t) = \mathbf{k} \cdot (\mathbf{x}_1 - \mathbf{x}_2) = k_{sp}L \cos \phi \\ &= k_{sp}L \cos(\omega_s t + \phi_0), \end{aligned} \quad (2)$$

where  $k_{sp}$  is the component of  $\mathbf{k}$  in the spin plane,  $L$  the effective distance between the two EFI probes,  $\omega_s$  the spin rate of the spacecraft, and  $\phi_0$  the initial phase of the spin. On the other hand, the time delay of waves moving from one EFI probe to the other is

$$\Delta t = \frac{L \cos \phi}{v_{sp}} = \frac{L}{v_{sp}} \cos(\omega_s t + \phi_0), \quad (3)$$

where  $\Delta t$  is the time delay, and  $v_{sp}$  is the spin plane component of the phase velocity of the waves. Equations (2) and (3) show that both  $\Delta\theta$  and  $\Delta t$  are a sinusoidal function of time with amplitudes as a function of wave number and

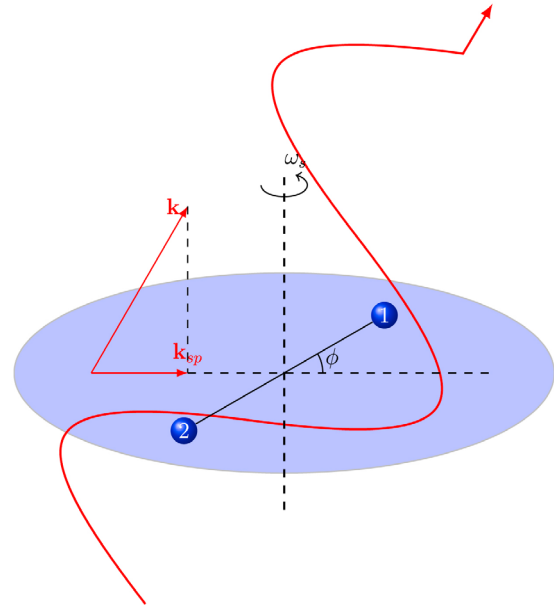


**Figure 4.** Illustration of waves passing an EFI boom. The blue balls, numbered 1 and 2, represent the two probes on an EFI boom in the spin plane (the light blue ellipse plane). The spin rate is  $\omega_s$ . The red, wave-like curve represents a series of waves passing the probes with wave vector  $\mathbf{k}$  whose spin plane component is  $k_{sp}$ . The angle between  $k_{sp}$  and the EFI boom is denoted with  $\phi$ .

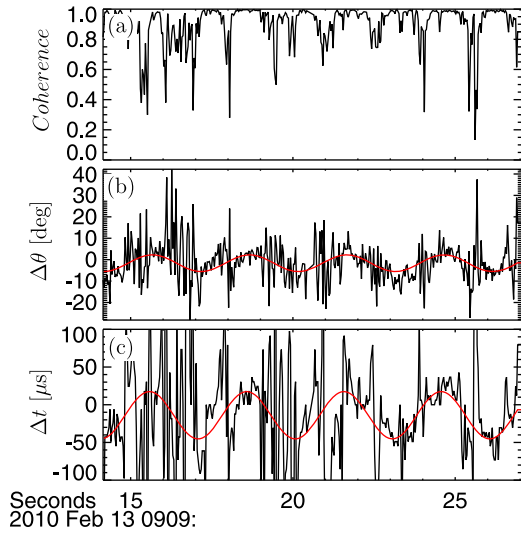


**Figure 5.** Cross-spectrum analysis and cross-correlation analysis results of WB1 using the EFI boom 1–2. (a) Coherence. (b) Phase shift ( $\Delta\theta$ ). The red line is a fit of  $\Delta\theta$  according to equation (2). (c) Time delay ( $\Delta t$ ). The red line is a fit of  $\Delta t$  according to equation (3).

phase velocity respectively. Therefore, by fitting the derived  $\Delta\theta$  and  $\Delta t$  from observations with a sinusoidal model, one can derive  $k_{sp}$  and  $v_{sp}$  from the amplitudes of the resultant fits.

[16] In this paper,  $\Delta\theta$  is obtained from cross-spectrum analysis and  $\Delta t$  from cross-correlation analysis. For a monochromatic wave, the two kinds of analysis are interchangeable if the wave frequency is known. However, in observations, there is a spread in both wave number and wave frequency, and hence these two analyses have different use, with the cross-spectrum analysis ideal for deriving wave number and the cross-correlation analysis ideal for deriving

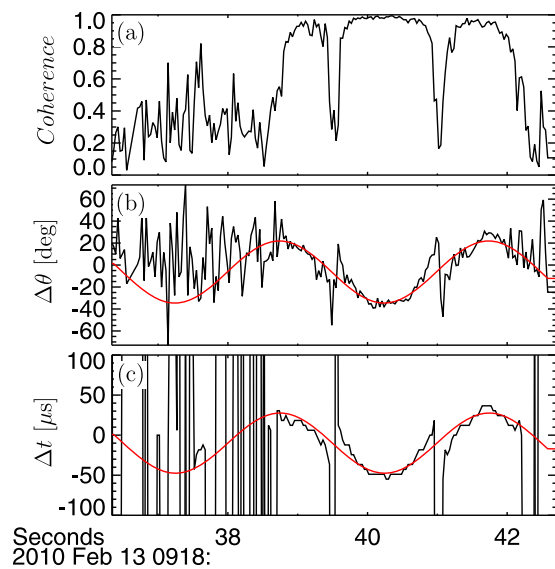


**Figure 6.** Cross-spectrum analysis and cross-correlation analysis results of WB2 using the EFI boom 1–2. The format is the same as Figure 5.

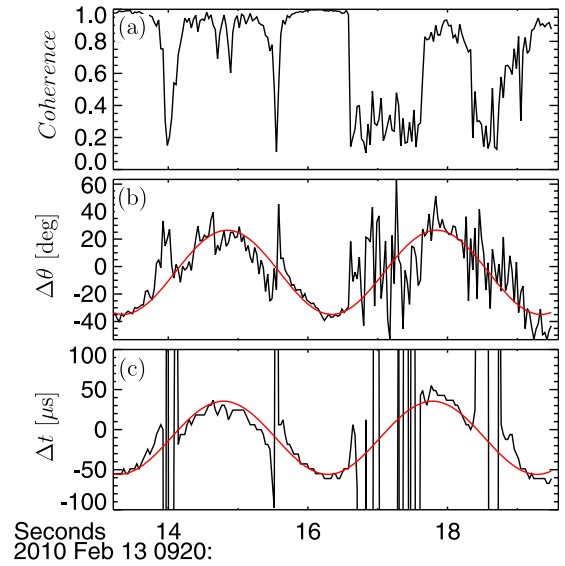


**Figure 7.** Cross-spectrum analysis and cross-correlation analysis results of WB3 using the EFI boom 1–2. The format is the same as Figure 5.

phase velocity. In cross-spectrum analysis, the derived phase shift is generally averaged over a number of frequency bins. Therefore, the resultant wavelength is an average over the corresponding frequencies. On the other hand, in cross-correlation analysis, it is assumed that the signals have a uniform velocity over a frequency range of interest in the timescale of  $\Delta t$ .

[17] In addition to  $\Delta\theta$ , the cross-spectrum analysis gives the coherence between two series of signals, which varies between 0 and 1. When the coherence is close to 1, it indicates that the two series of signals are coherent and hence favors the reliability of  $\Delta\theta$  and  $\Delta t$ .

[18] Figure 5 shows the coherence, phase shift, and time delay of WB1 derived from EFI voltage measurements. The voltage data are band-pass filtered from 100 to 700 Hz prior to analysis. The calculation of the coherence and phase shift uses 20 the most powerful frequency bins. (Each frequency bin has a band width of 8 Hz.) The red lines in Figures 5b and 5c are sinusoidal fits to  $\Delta\theta$  and  $\Delta t$ , respectively, using data points with coherence greater than 0.85. One can see that the data (the black line) generally follow the fits well when the coherence is close to 1, especially for  $\Delta t$  after 09:09:22 UT, indicating that  $k_{sp}$  and  $v_{sp}$  from the fits have a relatively high degree of reliability. The fits of  $\Delta\theta$  and  $\Delta t$  give  $k_{sp} = 0.001912 \text{ m}^{-1}$  and  $v_{sp} = 1131 \text{ km s}^{-1}$ , respectively, with uncertainties less than 30%. Assuming  $\mathbf{k} \parallel \mathbf{B}_0$ , this corresponds to a wavelength of 1727 m and a phase velocity of  $2151 \text{ km s}^{-1}$ , respectively.

**Table 1.** Parameters of Initial Electron Distribution

	Run 1	Run 2
$n_1$	1.01	1.015
$v_{t1}$	1	1
$n_b$	-0.01	-0.015
$v_{tb}$	0.05	0.1
$u_b$	0.4	0.4

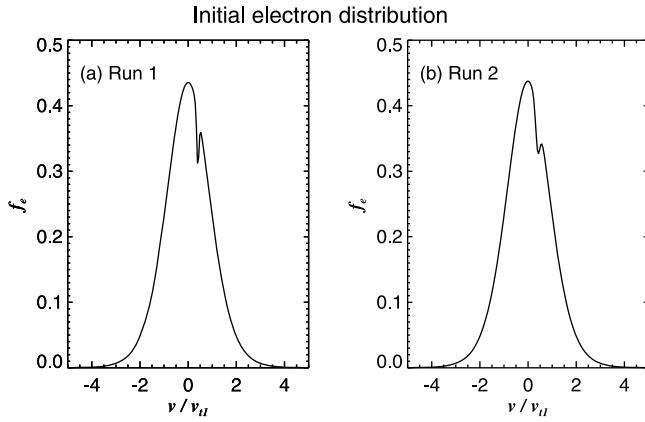


**Figure 8.** Initial electron distribution of runs 1 and 2.

[19] Figures 6 and 7 show the results of WB2 and WB3, respectively, in the same format of Figure 5. The voltage data are band-pass filtered from 1 to 3 kHz for both bursts. Compared to Figure 5, the fits of  $\Delta\theta$  and  $\Delta t$  show much better agreement with data when the coherence is close to 1 in Figures 6 and 7. With similar calculations, we obtain a wavelength of 272 m and a phase velocity of  $1568 \text{ km s}^{-1}$  for WB2, and a wavelength of 231 m and a phase velocity of  $1397 \text{ km s}^{-1}$  for WB3.

## 5. Wave Mode

[20] As shown in Figure 2f, the power enhancement in the electrostatic waves on the outbound side of the flyby generally lies between  $0.1f_{pe}$  and  $0.4f_{pe}$ . In this frequency range, the electron beam mode [Gary, 1985] and the electron acoustic mode [Gary and Tokar, 1985] are two possible candidates for driving wave growth. However, the latter

requires a substantial hot electron component, whose presence is not supported by observations. Thus, the observed electrostatic waves are likely to be the electron beam mode. To confirm this, we performed 1-D, electrostatic Vlasov simulations with the initial conditions close to observations so as to make relevant comparisons between simulations and observations. As shown later, the observed waves have different wavelengths in units of the local Debye length, namely, different values of  $k\lambda_D$  in WB1, WB2, and WB3. To cover the observed range of  $k\lambda_D$ , we present two representative runs with different values of  $k\lambda_D$  for the fastest growing mode.

[21] The Vlasov code we used is based on the time-splitting scheme of Cheng and Knorr [1976] with open boundary conditions. More details regarding the code can be found in Newman et al. [2008]. Ions are initialized as homogeneous, Maxwellian background with proton mass. Electrons are initialized with two components. The initial electron velocity distribution function takes the form

$$f_e(v) = \frac{n_1 \Gamma[\kappa]}{\sqrt{\pi(2\kappa-3)v_{t1}^2} \Gamma[\kappa-1/2]} \left(1 + \frac{v^2}{(2\kappa-3)v_{t1}^2}\right)^{-\kappa} + \frac{n_b \Gamma[\kappa]}{\sqrt{\pi(2\kappa-3)v_{tb}^2} \Gamma[\kappa-1/2]} \left(1 + \frac{(v-u_b)^2}{(2\kappa-3)v_{tb}^2}\right)^{-\kappa}, \quad (4)$$

where the one-dimensional kappa distribution [Summers and Thorne, 1991] is used with  $\kappa = 6$ ;  $\Gamma$  is the gamma function;  $n_1$  and  $v_{t1}$  are the number density and thermal velocity of the major background component respectively;  $n_b$ ,  $v_{tb}$ , and  $u_b$  are the number density, thermal velocity, and drifting velocity of the minor beam-like component, respectively.

[22] Table 1 lists parameters of initial electron distribution of the two runs. As shown in Figures 2c and 2e, the energy level of the enhanced parallel electron differential energy flux is approximately equal to the background electron temperature.

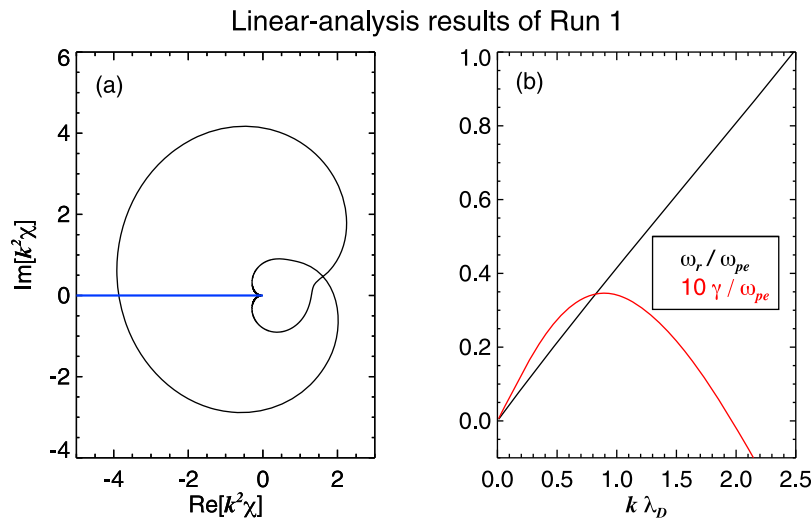


**Figure 9.** Linear analysis results of the initial electron distribution of run 1. (a) Nyquist diagram, where  $k$  is wave number,  $\chi$  is the regular susceptibility in an electrostatic, kinetic model, and the blue line represents the negative real axis. (b) The dispersion relation of electron beam mode, where  $\omega_r$  and  $\gamma$  are the real and the imaginary parts of the complex wave frequency, respectively, and  $\omega_{pe} = (n_0 e^2 / \epsilon_0 m_e)^{1/2}$ . The growth curve  $\gamma - k$  (the red line) is scaled by a factor of 10 for easy recognition.

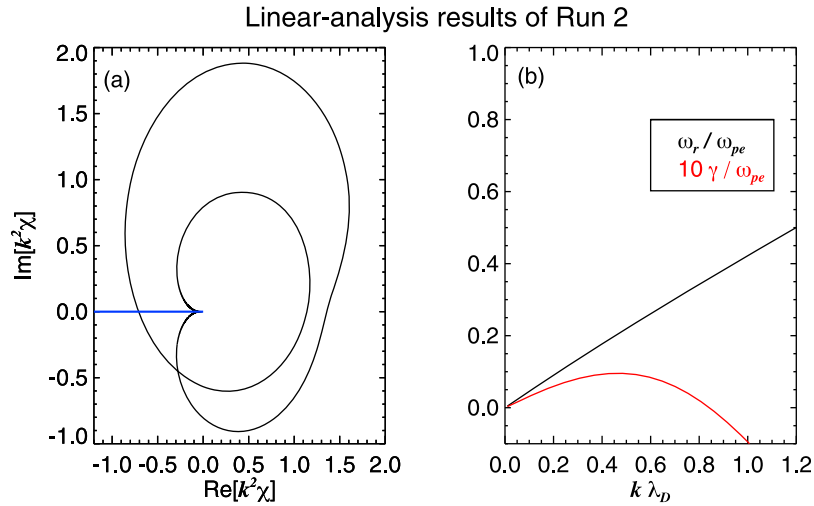


**Figure 10.** Linear-analysis results of the initial electron distribution of run 2. The format is the same as Figure 9.

However, because differential energy flux is proportional to  $E^2 f$ , where  $E$  and  $f$  represent energy and distribution function, respectively, the energy level of the beam is not equal to but a fraction of that of the enhanced differential energy flux. (At beam energy level ( $E_b$ ),  $\partial f / \partial E|_{E_b} = 0$ ; thus,  $\partial(E^2 f) / \partial E|_{E_b} = E^2(\partial f / \partial E) + 2E f = 2E_b f(E_b) > 0$ , indicating  $E_b$  is lower than the energy level of the peak differential energy flux where  $\partial(E^2 f) / \partial E = 0$ .) Thus,  $u_b$  is chosen to be a fraction of the thermal velocity of the background electrons for both runs, as shown in Table 1. For such a low drifting velocity, it is relatively easier to “carve” the distribution function than to add a bump to create a positive slope. Therefore, we use negative  $n_b$ . Due to the negative  $n_b$  and small  $v_{ib}$ , the initial beam velocity that corresponds to a positive peak in the distribution function is slightly larger than  $u_b$ . Figure 8 shows the profiles of initial electron distribution of runs 1 and 2.

[23] The phase space domain is distributed on a  $N_z \times N_{ve}(N_{vi}) = 4096 \times 2048(256)$  grid that spans the region  $0 \leq z \leq L_z = 4096 \lambda_D$  and  $-12v_{i1}(-10v_{ii}) \leq v \leq 12v_{i1}(10v_{ii})$ , where  $\lambda_D = \epsilon_0 m_e v_{i1}^2 / n_0 e^2$ ,  $n_0 = n_1 + n_2$ , and  $v_{i1}(v_{ii})$  is the thermal velocity of the background electrons (ions). The size of the simulation domain and the homogeneous initial density is sufficient to model the *local* wave dynamics considered here. A larger *global* simulation study that includes spatial inhomogeneity will be the subject of future investigation.

[24] Figure 9 shows linear analysis results of the initial electron distribution of run 1. In Figure 9a, the Nyquist curve crosses the negative real axis (the blue line) once, indicating that there is one unstable mode in the system [Penrose, 1960]. (The Nyquist curve starts and ends at the origin, which must be excluded when counting crossings of the negative real axis.) Figure 9b shows the dispersion relation of the unstable mode. The linear feature of the  $\omega_r - k$  relation (the black line) is consistent with the electron beam mode, as shown in previous studies [Gary, 1985; Onsager and Holzworth, 1990]. The  $\gamma - k$  relation (the red line) shows that the fastest growing mode has  $k \lambda_D \approx 0.8$ , with the growing modes extending to  $k \lambda_D \approx 2$ .

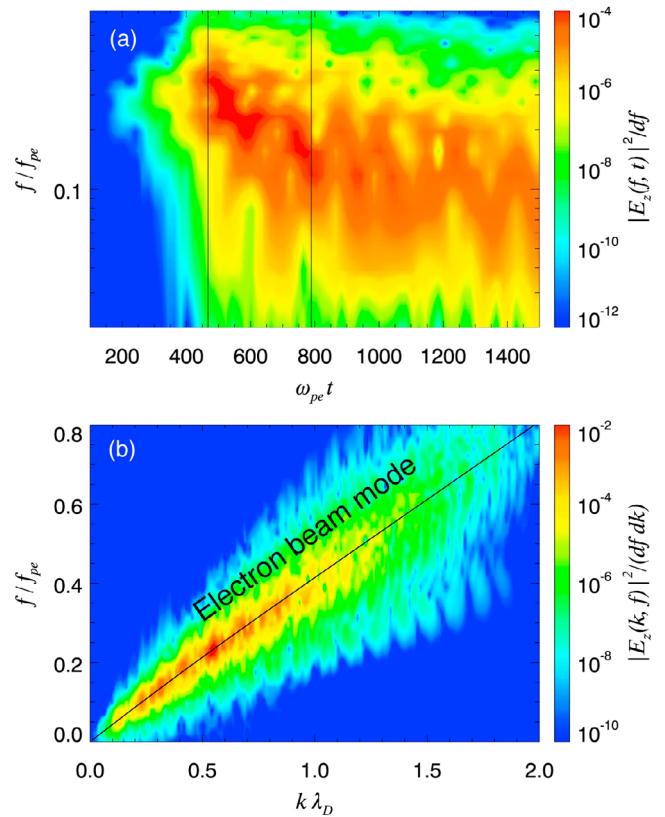


**Figure 11.** Spectral results of run 1. (a) Spectrogram of  $E_z$  at the center of the simulation box ( $z/L_z = 0.5$ ), where  $f_{pe} = \omega_{pe}/2\pi$ . (b) Frequency–wave number spectrum calculated from the period between the two vertical lines in Figure 11a, where the oblique black line is from the linear analysis of the initial electron distribution. The frequency range in Figure 11a is in a log scale for a close comparison with observations, whereas the frequency range in Figure 11b is in a linear scale to preserve the linear feature of the frequency–wave number relation of the electron beam mode.

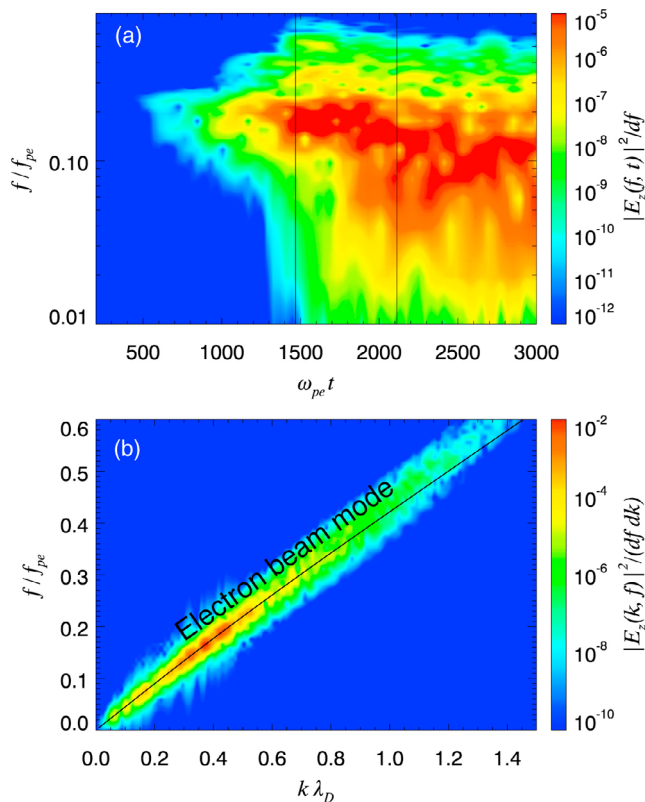


**Figure 12.** Spectral results of run 2. The format is the same as Figure 11.

[25] Figure 10 shows linear analysis results of the initial electron distribution of run 2. The results are generally similar to those of run 1 except that the fastest growing mode has  $k\lambda_D \approx 0.45$  in run 2. We performed a linear analysis for a set of initial parameters, and found that the  $k\lambda_D$  of the fastest growing mode is most sensitive to  $v_{tb}$ , which is somewhat expected since  $v_{tb}$  affects the positive slope in the initial distribution most. The general trend is that the smaller the  $v_{tb}$ , or the steeper the positive slope in the initial distribution, the larger the  $k\lambda_D$  of the fastest growing mode. For the three wave bursts WB1, WB2, and WB3, the local values of  $\lambda_D$  are roughly 108, 53, and 46 m, respectively, and the corresponding values of  $k\lambda_D$  are roughly 0.4, 1.23, and 1.24, respectively, with the wavelengths derived in section 4. All the observed  $k\lambda_D$  are accessible for electron beam mode based on our linear analysis results.

[26] Figure 11 shows spectral results of run 1. As shown in Figure 11a, the frequency of the waves is around  $0.2f_{pe}$ , consistent with the higher-frequency part of the spectrum in Figure 2f. The frequency–wave number spectrum in Figure 11b matches the linear analysis result of electron beam mode quite well, supporting that the observed frequency-time spectrum in Figure 2f is likely on the electron beam mode branch. Figure 12 shows spectral results of run 2, which generally supports the same conclusion from Figure 11.

## 6. Discussion and Summary

[27] The amplitudes of electric field waveforms in WB1 are clearly more modulated than those in WB2 and WB3 as

shown in Figure 3, suggesting that other wave modes may be involved in WB1. As shown in Figure 2f, the wave frequency spectrum at the time of WB1 has a low-frequency component that can reach as low as  $0.01f_{pe}$ , a value that is below the frequency range of the electron beam mode. The location of WB1 coincided with the minimum density shown in Figure 2a, indicating that the spacecraft was relatively deep inside the wake at the time. Similar to *Ogilvie et al.* [1996], *Halekas et al.* [2011] reported counter-streaming ions in the wake. Because  $0.01f_{pe}$  is on the order of ion plasma frequency, ion dynamics may be involved in WB1. In addition, WB1 spans a broader frequency band than WB2 and WB3. Previous studies show that both solitary structure (e.g., electron phase space holes [Kojima et al., 1997]) and nonsolitary structures (e.g., chorus emissions [Santolik et al., 2003]) can produce a broadband spectrum. In our case, no well-defined solitary structures are present in WB1 or in the simulations. The fact that WB1 presents more complex features than WB2 and WB3 suggests that the plasma dynamics deep inside the wake is likely more complicated than that close to wake boundaries, and more thorough kinetic studies are needed to address the complexity of WB1.

[28] Since the waves in WB1 likely consist of wave modes other than just the electron beam mode, it is difficult to make pertinent comparisons of the amplitudes of the waveforms between simulations and observations for WB1. However, the wave energy of WB2 and WB3 is mostly within the frequency range of the electron beam mode, and thus a waveform amplitude comparison between simulations and observations would be appropriate for these two bursts. Since run 1 has  $k\lambda_D (\sim 1.0)$ , which is closer to those in WB2 (1.23) and WB3 (1.24), than does run 2 ( $\sim 0.4$ ), we use run 1 to make such a comparison. In the simulation, the electric field is normalized by  $e\lambda_D n_0 / \epsilon_0$ , i.e.,  $E = (e\lambda_D n_0 / \epsilon_0) \tilde{E}$ , where  $E$  is the electric field in physical units, and  $\tilde{E}$  is the normalized electric field in the simulation. For WB2 and WB3,  $\lambda_D \sim 50$  m,  $n_0 \sim 0.5$  cm $^{-3}$ ; the amplitude of the normalized  $E_z$  in run 1 is roughly 0.005. Therefore, given parameters of WB2 and WB3, the simulation gives an electric field amplitude of roughly 2 mV m $^{-1}$ . Considering the uncertainties in modeling the unstable distribution function, the simulation result for the electric field amplitude is in a fairly good agreement with the observations as shown in Figures 3c and 3e.

[29] Kinetic instabilities have been observed in previous simulations of the lunar wake. *Farrell et al.* [1998] showed electrostatic instabilities in the wake with 1-D PIC simulations, although they did not further address the nature of the electrostatic instabilities. *Birch and Chapman* [2001a, 2001b, 2002] observed nonlinear electrostatic waves, namely, electron phase space holes [Roberts and Berk, 1967; Singh et al., 2011], in 1-D and 2-D PIC simulations of the wake.

[30] In addition to simulation work, *Bale* [1997] studied the effects of the absorption of solar wind plasmas by the lunar surface and proposed that the positive slope of the affected electron distribution might be responsible for the Langmuir waves observed by Wind during a period when the spacecraft was magnetically connected to the lunar wake [Bale et al., 1997]. However, for this flyby, *Halekas et al.* [2011] suggested that the observed electrostatic

waves may be due to the filtration of the electron distribution by the wake potential.

[31] In summary, we showed the characteristics of the observed electrostatic waves, in particular, the wavelength and phase velocity measurements from cross-spectrum analysis and cross-correlation analysis of EFI data. The estimated wavelengths vary from a few hundred meters to a couple of thousand meters, whereas the estimated phase velocities are on the order of  $1000 \text{ km s}^{-1}$ . Finally, we used a 1-D Vlasov code to identify the mode of those electrostatic waves and concluded that those waves were likely the electron beam mode.

[32] **Acknowledgments.** The entire THEMIS/ARTEMIS team is gratefully acknowledged. This work was funded by NASA grants for THEMIS and a NASA Earth and Space Sciences Fellowship (10-Helio10F-0004, 11-Helio11R-0001). NSF grant ATM-0714621 is acknowledged. Financial support for the FGM Lead Investigator Team at the Technical University of Braunschweig by the German Ministerium für Wirtschaft und Technologie and the Deutsches Zentrum für Luft- und Raumfahrt under grant 50OC1001 is acknowledged. We acknowledge A. Roux and O. Le Contel for use of SCM data.

[33] Masaki Fujimoto thanks the reviewers for their assistance in evaluating this paper.

## References

- Angelopoulos, V. (2008), The THEMIS Mission, *Space Sci. Rev.*, *141*, 5–34, doi:10.1007/s11214-008-9336-1.
- Angelopoulos, V. (2010), The ARTEMIS Mission, *Space Sci. Rev.*, doi:10.1007/s11214-010-9687-2, in press.
- Angelopoulos, V., F. S. Mozer, J. Bonnell, M. Temerin, M. Somoza, W. K. Peterson, H. L. Collin, and B. Giles (2001), Wave power studies of cusp crossings with the Polar satellite, *J. Geophys. Res.*, *106*, 5987–6006, doi:10.1029/2000JA900127.
- Auster, H. U., et al. (2008), The THEMIS fluxgate magnetometer, *Space Sci. Rev.*, *141*, 235–264, doi:10.1007/s11214-008-9365-9.
- Bale, S. D. (1997), Shadowed particle distributions near the Moon, *J. Geophys. Res.*, *102*, 19,773–19,778, doi:10.1029/97JA01676.
- Bale, S. D., C. J. Owen, J.-L. Bougeret, K. Goetz, P. J. Kellogg, R. P. Lepping, R. Manning, and S. J. Monson (1997), Evidence of currents and unstable particle distributions in an extended region around the lunar plasma wake, *Geophys. Res. Lett.*, *24*, 1427–1430, doi:10.1029/97GL01193.
- Birch, P. C., and S. C. Chapman (2001a), Particle-in-cell simulations of the lunar wake with high phase space resolution, *Geophys. Res. Lett.*, *28*, 219–222, doi:10.1029/2000GL011958.
- Birch, P. C., and S. C. Chapman (2001b), Correction to “Particle-in-cell simulations of the lunar wake with high phase space resolution,” *Geophys. Res. Lett.*, *28*(13), 2669, doi:10.1029/2001GL012961.
- Birch, P. C., and S. C. Chapman (2002), Two dimensional particle-in-cell simulations of the lunar wake, *Phys. Plasmas*, *9*, 1785–1789, doi:10.1063/1.1467655.
- Bonnell, J. W. (1997), Identification of broadband ELF waves observed during transverse ion acceleration in the auroral ionosphere, Ph.D. thesis, Cornell Univ., Ithaca, N. Y.
- Bonnell, J. W., F. S. Mozer, G. T. Delory, A. J. Hull, R. E. Ergun, C. M. Cully, V. Angelopoulos, and P. R. Harvey (2008), The Electric Field Instrument (EFI) for THEMIS, *Space Sci. Rev.*, *141*, 303–341, doi:10.1007/s11214-008-9469-2.
- Bosqued, J. M., et al. (1996), Moon-solar wind interaction: First results from the WIND/3DP experiment, *Geophys. Res. Lett.*, *23*, 1259–1262, doi:10.1029/96GL00303.
- Cheng, C. Z., and G. Knorr (1976), The integration of the Vlasov equation in configuration space, *J. Comput. Phys.*, *22*, 330–351, doi:10.1016/0021-9991(76)90053-X.
- Cully, C. M., R. E. Ergun, K. Stevens, A. Nammari, and J. Westfall (2008), The THEMIS Digital Fields Board, *Space Sci. Rev.*, *141*, 343–355, doi:10.1007/s11214-008-9417-1.
- Ergun, R. E., E. Klemmentis, C. W. Carlson, J. P. McFadden, and J. H. Clemmons (1991), Wavelength measurement of auroral hiss, *J. Geophys. Res.*, *96*, 21,299–21,307, doi:10.1029/91JA01863.
- Farrell, W. M., R. J. Fitzenreiter, C. J. Owen, J. B. Byrnes, R. P. Lepping, K. W. Ogilvie, and F. Neubauer (1996), Upstream ULF waves and energetic electrons associated with the lunar wake: Detection of precursor activity, *Geophys. Res. Lett.*, *23*, 1271–1274, doi:10.1029/96GL01355.
- Farrell, W. M., M. L. Kaiser, J. T. Steinberg, and S. D. Bale (1998), A simple simulation of a plasma void: Applications to Wind observations of the lunar wake, *J. Geophys. Res.*, *103*, 23,653–23,660, doi:10.1029/97JA03717.
- Feldman, W. C., J. R. Asbridge, S. J. Bame, M. D. Montgomery, and S. P. Gary (1975), Solar wind electrons, *J. Geophys. Res.*, *80*, 4181–4196, doi:10.1029/JA080i031p04181.
- Gary, S. P. (1985), Electrostatic instabilities in plasmas with two electron components, *J. Geophys. Res.*, *90*, 8213–8221.
- Gary, S. P., and R. L. Tokar (1985), The electron-acoustic mode, *Phys. Fluids*, *28*, 2439–2441, doi:10.1063/1.865250.
- Halekas, J. S., et al. (2011), First results from ARTEMIS, a new Two-spacecraft lunar mission: Counter-streaming plasma populations in the lunar wake, *Space Sci. Rev.*, doi:10.1007/s11214-010-9738-8, in press.
- Kallio, E. (2005), Formation of the lunar wake in quasi-neutral hybrid model, *Geophys. Res. Lett.*, *32*, L06107, doi:10.1029/2004GL021989.
- Kellogg, P. J., K. Goetz, S. J. Monson, J. Bougeret, R. Manning, and M. L. Kaiser (1996), Observations of plasma waves during a traversal of the Moon’s wake, *Geophys. Res. Lett.*, *23*, 1267–1270, doi:10.1029/96GL00376.
- Kojima, H., H. Matsumoto, S. Chikuba, S. Horiyama, M. Ashour-Abdalla, and R. R. Anderson (1997), Geotail waveform observations of broadband/narrowband electrostatic noise in the distant tail, *J. Geophys. Res.*, *102*, 14,439–14,456, doi:10.1029/97JA00684.
- Labelle, J., and P. M. Kintner (1989), The measurement of wavelength in space plasmas, *Rev. Geophys.*, *27*, 495–518, doi:10.1029/RG027i004p00495.
- Louarn, P., et al. (2009), On the temporal variability of the “strahl” and its relationship with solar wind characteristics: STEREO SWEA observations, *Solar Phys.*, *259*, 311–321, doi:10.1007/s11207-009-9402-1.
- McFadden, J. P., C. W. Carlson, D. Larson, M. Ludlam, R. Abiad, B. Elliott, P. Turin, M. Marckwordt, and V. Angelopoulos (2008), The THEMIS ESA plasma instrument and in-flight calibration, *Space Sci. Rev.*, *141*, 277–302, doi:10.1007/s11214-008-9440-2.
- Nakagawa, T., Y. Takahashi, and M. Iizima (2003), GEOTAIL observation of upstream ULF waves associated with lunar wake, *Earth Planets Space*, *55*, 569–580.
- Ness, N. F. (1972), Interaction of the solar wind with the Moon, in *The Interplanetary Medium: Part II of Solar-Terrestrial Physics/1970*, edited by E. R. Dyer, J. G. Roederer, and A. J. Hundhausen, pp. 159–205, D. Reidel, Dordrecht, Netherlands.
- Ness, N. F., K. W. Behannon, C. S. Scearce, and S. C. Cantarano (1967), Early results from the magnetic field experiment on Lunar Explorer 35, *J. Geophys. Res.*, *72*, 5769–5778, doi:10.1029/JZ072i023p05769.
- Newman, D. L., L. Andersson, M. V. Goldman, R. E. Ergun, and N. Sen (2008), Influence of suprathermal background electrons on strong auroral double layers: Vlasov-simulation parameter study, *Phys. Plasmas*, *15*(7), 072902, doi:10.1063/1.2938753.
- Ogilvie, K. W., J. T. Steinberg, R. J. Fitzenreiter, C. J. Owen, A. J. Lazarus, W. M. Farrell, and R. B. Torbert (1996), Observations of the lunar plasma wake from the WIND spacecraft on December 27, 1994, *Geophys. Res. Lett.*, *23*, 1255–1258, doi:10.1029/96GL01069.
- Onsager, T. G., and R. H. Holzworth (1990), Measurement of the electron beam mode in Earth’s foreshock, *J. Geophys. Res.*, *95*, 4175–4186, doi:10.1029/JA095iA04p04175.
- Owen, C. J., R. P. Lepping, K. W. Ogilvie, J. A. Slavin, W. M. Farrell, and J. B. Byrnes (1996), The lunar wake at  $6.8 R_L$ : WIND magnetic field observations, *Geophys. Res. Lett.*, *23*, 1263–1266, doi:10.1029/96GL01354.
- Pedersen, A., F. Mozer, and G. Gustafsson (1998), Electric field measurements in a tenuous plasma with spherical double probes, in *Measurement Techniques in Space Plasmas: Fields*, *Geophys. Monogr. Ser.*, vol. 103, edited by R. F. Pfaff, J. E. Borovsky, and D. T. Young, pp. 1–12, AGU, Washington, D. C.
- Penrose, O. (1960), Electrostatic instabilities of a uniform non-Maxwellian plasma, *Phys. Fluids*, *3*, 258–265, doi:10.1063/1.1706024.
- Roberts, K. V., and H. L. Berk (1967), Nonlinear evolution of a two-stream instability, *Phys. Rev. Lett.*, *19*, 297–300, doi:10.1103/PhysRevLett.19.297.
- Roux, A., O. Le Contel, C. Coillot, A. Bouabdellah, B. de La Porte, D. Alison, S. Ruocco, and M. C. Vassal (2008), The search coil magnetometer for THEMIS, *Space Sci. Rev.*, *141*, 265–275, doi:10.1007/s11214-008-9455-8.
- Samir, U., K. H. Wright Jr., and N. H. Stone (1983), The expansion of a plasma into a vacuum: Basic phenomena and processes and applications to space plasma physics, *Rev. Geophys.*, *21*(7), 1631–1646, doi:10.1029/RG021i007p01631.
- Santolík, O., D. A. Gurnett, J. S. Pickett, M. Parrot, and N. Cornilleau-Wehrin (2003), Spatio-temporal structure of storm-time chorus, *J. Geophys. Res.*, *108*(A7), 1278, doi:10.1029/2002JA009791.

- Schubert, G., and B. R. Lichtenstein (1974), Observations of Moon-plasma interactions by orbital and surface experiments, *Rev. Geophys.*, *12*(4), 592–626, doi:10.1029/RG012i004p00592.
- Singh, N., S. Araveti, and E. B. Wells (2011), Mesoscale PIC simulation of double layers and electron holes affecting parallel and transverse accelerations of electrons and ions, *J. Geophys. Res.*, *116*, A00K09, doi:10.1029/2010JA016323.
- Summers, D., and R. M. Thorne (1991), The modified plasma dispersion function, *Phys. Fluids B*, *3*, 1835–1847, doi:10.1063/1.859653.
- Wiehle, S., et al. (2011), First lunar wake passage of ARTEMIS: Discrimination of wake effects and solar wind fluctuations by 3D hybrid simulations, *Planet. Space Sci.*, *59*, 661–671, doi:10.1016/j.pss.2011.01.012.
- L. Andersson, R. E. Ergun, and J. B. Tao, Laboratory for Atmospheric and Space Physics, University of Colorado at Boulder, 1234 Innovation Dr., Boulder, CO 80303-7814, USA. (jianbao.tao@colorado.edu)
- V. Angelopoulos, IGPP/ESS, University of California, Box 951567, 2712 Geology Bldg., Los Angeles, CA 90095-1567, USA.
- H.-U. Auster and K.-H. Glassmeier, Institut für Geophysik und Extraterrestrische Physik, Technische Universität Braunschweig, Mendelssohnstr. 3, D-38106 Braunschweig, Germany.
- W. Baumjohann, Space Research Institute, Austrian Academy of Sciences, Schmiedlstr. 6, A-8042 Graz, Austria.
- J. W. Bonnell, J. S. Halekas, D. E. Larson, and J. P. McFadden, Space Sciences Laboratory, University of California, 7 Gauss Way, Berkeley, CA 94720-7450, USA.
- C. M. Cully, Swedish Institute of Space Physics, Box 537, SE-751 21 Uppsala, Sweden.
- M. V. Goldman and D. L. Newman, Center for Integrated Plasma Studies, University of Colorado at Boulder, UCB 390, Boulder, CO 80309-0390, USA.